

# Shocks in Ion Sputtering Sharpen Steep Surface Features

H. Henry Chen,<sup>1\*</sup> Omar A. Urquidez,<sup>2</sup> Stefan Ichim,<sup>2</sup>  
L. Humberto Rodriquez,<sup>2</sup> Michael P. Brenner,<sup>2</sup> Michael J. Aziz<sup>2,†</sup>

We report a regime of ion beam sputtering that occurs for sufficiently steep slopes. High slopes propagate over large distances without dissipating the steepest features. Both the propagation velocity and the dynamically selected slope are universal, independent of the details of the initial shape of the surface. The resulting behavior can be understood as the propagation of a shock front that self-selects a stable slope, as has been previously observed in thin-film fluid flows. Experiments confirm predictions of the theory. An important implication of the propagative behavior at high surface slopes is that a pattern can be fabricated at a large length scale and, through uniform ion irradiation, reduced to a smaller length scale while preserving, or even sharpening, the sharpest features.

Methods of micro- and nanofabrication of three-dimensional (3D) structures are of increasing interest owing to their importance for the creation of compact 3D devices and their assembly into functional 3D systems. Examples include microelectromechanical systems, 3D integration of electronic microprocessors, 3D information storage, and photonic band gap waveguides. Ion beam irradiation of steeply sloping surfaces has been used for micromachining tall, steep features (1, 2); fabricating semiconductor quantum dots through a self-organization process (3, 4); templating for guided self-organization of sputter patterns (5); and ion beam sculpting of nanopore single-biomolecule detectors (6, 7). Because ion irradiation is currently used for doping control in the mass production of semiconductor devices, there may be little impediment to its rapid uptake for morphology control if the predictability is improved.

The theory of ion sputtering (8, 9) has been applied to nearly flat surfaces and has received a great deal of attention in the context of pattern-forming morphological instabilities (3, 4, 10–19). However, current theories expand the sputtering behavior in powers of surface slope and are restricted to small slopes, and thus comparisons of theory and experiment have focused on small-slope evolution. Through theory, experiments, and computer simulations, we have discovered a new regime of ion beam sputtering that occurs for sufficiently steep slopes. High slopes propagate over large distances without dissipating the steepest features. Both the propagation velocity and the dynamically selected slope are universal, independent of the details of the initial shape of the surface.

Our theoretical results make use of the classical theory of sputtering (8, 9) and develop a small-curvature approximation that is valid for any slope. The resulting behavior can be understood as the propagation of a shock front that self-selects a stable slope; the mathematical structure of the solutions is the same as that previously observed in thin-film fluid flows (20, 21). An important implication of the propagative behavior at high surface slopes is that a pattern can be fabricated at a large length scale and, through uniform ion irradiation, reduced to a smaller length scale while preserving, or even sharpening, the sharpest features.

Our experiments use a focused ion beam (FIB) of 30-keV gallium to sputter a silicon target. The FIB is rastered over a rectangular region containing prefabricated pits of various depths and lateral dimensions. Surprisingly, the pits are not smeared out by the sputtering, but rather expand at fixed rates while maintaining steep walls throughout the expansion (Fig. 1). Crystallographic anisotropy is not a possible origin of this effect, because the surface becomes amorphous during the initial stage of ion implantation.

What is the mechanism for maintaining the sharp fronts? The simplest possibility is that it arises from the standard picture of sputtering due to Sigmund (8, 9), which posits that

as an average ion penetrates the surface a distance  $a$  parallel to its initial flight trajectory, its kinetic energy is distributed via collisions in a Gaussian ellipsoid with longitudinal and lateral widths  $\sigma$  and  $\mu$ , respectively. The probability that a surface atom is ejected is proportional to the total energy that reaches it from all ion bombardments. Redeposition of surface atoms is assumed to be negligible.

To test this hypothesis, we solve numerically a model combining Sigmund's mechanism with surface diffusion. Because the radius of the pit in the experiments is much larger than the scale over which the surface slope varies, we consider the edge of the pit as straight and track the evolution of its cross-sectional profile, described by the height function  $z = h(x, t)$ . We orient the  $z$  axis along the ion beam, with the ions impinging in the downward direction. The dynamics can then be written as an integral-differential equation for the rate at which the surface retracts in the locally normal direction

$$-\frac{\partial h/\partial t}{\sqrt{1+h_x^2}} = pJ\epsilon \int dx' E(x; x') - B\nabla^2 \kappa \quad (1)$$

The first term on the right represents sputtering, where  $J$  is the ion flux,  $p$  is the sputtering rate per unit power density,  $\epsilon$  is the energy released per ion, and  $E(x; x')$  is the normalized distribution of energy on the surface at  $x$  due to an ion bombardment at  $x'$ . The second term on the right describes surface diffusion (22) for a surface with mean curvature  $\kappa$  (reckoned positive for concave surfaces), with  $B$  a phenomenological constant; the classical equilibrium microscopic description of  $B$  (22) might be modified during sputtering. The collision parameters ( $a, \sigma, \mu$ ) can be obtained either through atomistic simulations (23) or through fits of sputter yield as a function of angle for a flat surface [SOM Text, Sect. 1.1 (24)].

Numerical solutions (“simulations”) of Eq. 1 show two different regimes, depending on the initial maximum slope of the pit. When the inclination angle of the initial pit wall is above the critical value of  $\approx 68^\circ$ , the leading edge of the profile evolves to a constant slope region (inclination  $\approx 76^\circ$ ) moving with a constant speed,

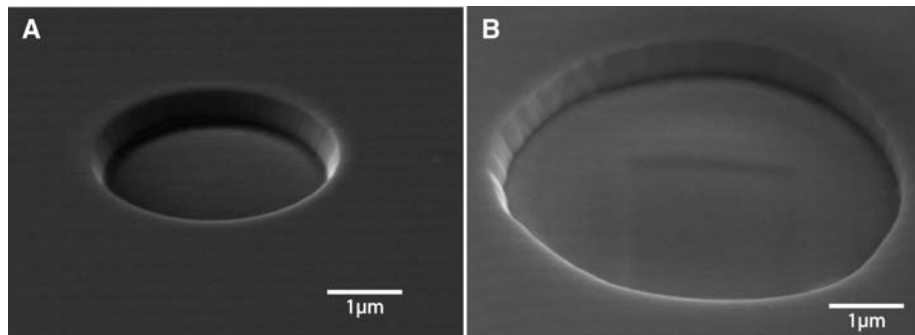


**Fig. 1.** (A) An SEM image of an initial circular pit in silicon with 3- $\mu\text{m}$  diameter and 0.5- $\mu\text{m}$  depth. (B) The wall of the enlarged pit is still sharp after uniform ion exposure to a fluence of  $\sim 1.5 \times 10^{19}$  ions/cm<sup>2</sup>.

<sup>1</sup>Department of Physics, <sup>2</sup>Division of Engineering and Applied Sciences, Harvard University, Cambridge, MA 02138, USA.

\*Present address: Lawrence Livermore National Laboratory, Livermore, CA 94550, USA.

†To whom correspondence should be addressed. E-mail: maziz@harvard.edu

in units of distance per unit fluence (Fig. 2A). Behind the leading edge there is a “snail’s foot,” which grows with time and gradually invades the constant slope region. Notably, both the velocity and the slope at the leading edge are universal, independent of the initial shape of the pit. Different initial conditions lead to quantitatively identical behaviors (compare Fig. 2, A and B). In contrast, if the initial maximum inclination is below the critical value, both the slope and the velocity continuously decrease: The steep edge dissipates.

We seek to understand why these regimes exist, by reducing Eq. 1 to a nonlinear partial differential equation that is more amenable to analysis. Previous reductions [e.g., (19)] have focused on surface modulations that are small relative to the ion penetration depth and hence are not suited for the evolution of tall and steep morphological features such as step edges. Instead, we note that although the slopes occurring in the solutions depicted in Fig. 1 are high, the length scale  $l$  over which the slope changes is in fact large compared to the penetration depth  $a$ . This motivated

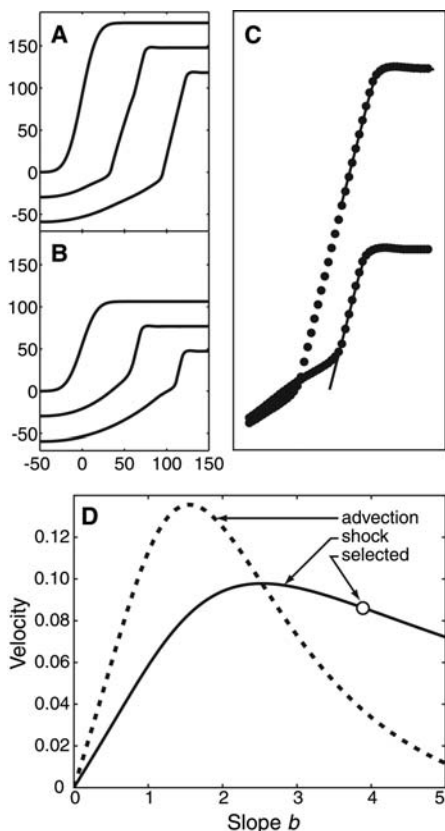


**Fig. 2.** Predicted profile evolution. (A and B) Time sequences showing evolution of  $h(x)$  starting from two different initial conditions. The maximum initial slope in (A) is 5.0 and in (B) is 3.0; the final slope for each is 3.9. (C) Each final profile agrees with the same similarity solution (solid line). (D) Comparison of the shock velocity  $U$  and the advection velocity  $C$  as functions of slope. An undercompressive shock solution exists at  $b = 3.9$ , indicated by the circle. Distances are normalized by  $\sigma$  and velocities are normalized by  $pJ\epsilon/\sigma$ .

us to carry out an expansion for the Sigmund integral in Eq. 1 in terms of the ratio  $a/l$  [SOM Text, Sect. 1.2 (24)], leading to

$$\frac{\partial h}{\partial t} = -Y(b) + D(b)\frac{\partial^2 h}{\partial x^2} + B\frac{\partial^2 \kappa}{\partial s^2} \quad (2)$$

where  $b \equiv \partial h/\partial x$ . This expansion shows that the Sigmund mechanism reduces to two simple (nonlinear) physical effects.  $Y(b)$  represents the erosion rate of a surface of constant slope  $b$ : Steeper surfaces erode faster than shallow ones because energy is deposited closer to the surface. The curvature coefficient  $D(b)$  is the origin of the celebrated Bradley-Harper instability (10): At small  $b$ ,  $D(b) < 0$ , causing concave regions to erode faster than convex regions. The instability is opposed by surface diffusion, as characterized by the final term in Eq. 2 and described in the SOM Text, Sect. 1.3 (24). Note the differentiation with respect to the arclength  $s$ .

Numerical comparison of solutions to both the reduced dynamics (Eq. 2) and the full Sigmund model (Eq. 1) shows that Eq. 2 quantitatively reproduces the full simulations [SOM Text, Sect. 1.4 (24)]. The terms in Eq. 2 that are most important for the traveling step are the erosion rate  $Y(b)$  and surface diffusion: The curvature effect  $D(b)$  is small and can be neglected without significant error. To make further progress, it is particularly illuminating to drop the curvature term and differentiate Eq. 2:

$$\frac{\partial b}{\partial t} + C\frac{\partial b}{\partial x} = B\frac{\partial}{\partial x}\frac{\partial^2 \kappa}{\partial s^2} \quad (3)$$

The left-hand side of the equation now has the canonical mathematical structure of a nonlinear conservation law (25), with  $C(b) \equiv (\partial/\partial b)Y(b)$  playing the role of a local advection velocity. Equations of this form arise in many physical contexts and typically result in nonlinear waves, such as shocks or rarefaction waves. The nonlinear dependence of the advection velocity on surface slope can lead to sharpening, which is counteracted by surface diffusion.

To understand when steps can propagate without dissipation, we seek solutions of Eq. 3 of the form  $b(x,t) = S(x - Ut)$ , where  $U$  is the propagation velocity. The numerical simulations indicate the solutions have zero slope on the right [ $b(x \rightarrow \infty) \rightarrow 0$ ] and fixed positive slope on the left [ $b(x \rightarrow -\infty) \rightarrow b_-$ ]. Equation 3 then implies [SOM Text, Sect. 1.5 (24)]

$$U = \frac{Y(b_-) - Y(0)}{b_-} \quad (4)$$

In shock dynamics, Eq. 4 is referred to as the Rankine-Hugoniot condition. For classical shocks, the shock velocity  $U$  satisfies the Lax condition  $C(b_-) > U > C(0) = 0$ : The advection velocity of the rear (front) of the shock is faster (slower) than the shock speed, and the profile is “compressed” from both sides. Figure 2D shows both the shock velocity

and the advection velocity. For slopes below  $b_- = 2.5$  or inclination angles below  $68^\circ$ , the Lax condition holds; hence, there is a continuous family of steady shock solutions over this range. However, for  $b_- > 2.53$ , the trailing edge of a putative shock is slower than the shock speed, which suggests that the shock would continuously spread in time.

Nonetheless, when the Lax condition is violated, steady shocks can still exist, as long as the dominant mechanism of smoothing is fourth-order diffusion (in this case, surface diffusion). However, such undercompressive shocks (26, 27) exist only if  $b_-$  is chosen to be a particular value. This result can be derived [SOM Text, Sect. 1.5 (24)] by determining the conditions under which solutions to the ordinary differential equation for the shock profile  $S(x - Ut) = S(\eta)$  are compatible with the boundary conditions.

Motivated by this argument, we conducted a numerical search for the selected velocity of the undercompressive shock and found that such a solution exists for  $b_- = 3.9$  ( $\theta = 76^\circ$ ) and  $U = 0.085(pJ\epsilon/\sigma)$ . Figure 2C shows that this solution agrees with numerical simulations of Eq. 1. The ratio of the shock velocity to the downward velocity of the sputtered surface at normal incidence is a fixed constant:  $U_{\text{shock}}/U_{\text{sputter}} = 1.7$ . This dimensionless number depends only on the shape of  $Y(b)$  through the parameters  $a/\sigma$  and  $\mu/\sigma$ . The surface diffusion parameter  $B$  does not affect the selected slope and velocity:  $B$  affects only the scale  $\sim B^{1/3}$  over which the slope changes from  $b_-$  to 0. Hence, the essential slope-steepening mechanism is independent of the surface diffusivity, as long as the dominant diffusive fluxes are fourth order.

To test this theory, we fabricated and then observed the subsequent evolution of pits in Si(001) at room temperature using a FEI DualBeam DB235 FIB-scanning electron microscope (SEM). We used a beam of  $\text{Ga}^+$  at 30 keV and 3 nA to machine rectangular pits (the “original fabrication pit” in Fig. 3) with lateral dimensions  $25 \mu\text{m}$  by  $12 \mu\text{m}$ . To minimize the effects of deposition of material sputtered from one pit edge onto another edge during subsequent evolution experiments, the pits straddled the cleaved edge of the Si wafer, so there was no opposite edge facing the “experimental edge” parallel to the cleaved boundary (Fig. 3). We milled rectangular pits with vertical side walls  $\sim 1.7 \mu\text{m}$  deep. For subsequent evolution, we irradiated the experimental edge with a rastered ( $20 \mu\text{m}$  by  $20 \mu\text{m}$ ) rectangle (the “evolution pit”) shorter than the edge length and extending farther from the cleavage edge than the original fabrication pit (Fig. 3). Irradiation was carried out in a vacuum of  $\approx 3 \times 10^{-6}$  mbar. The beam current was 3 nA and the spot size was nominally 60 nm. During rastering the beam dwells at each discrete location for  $1 \mu\text{s}$  and then moves rapidly to an adjacent location. The separation between adjacent locations was set to nominally 50% overlap, which in

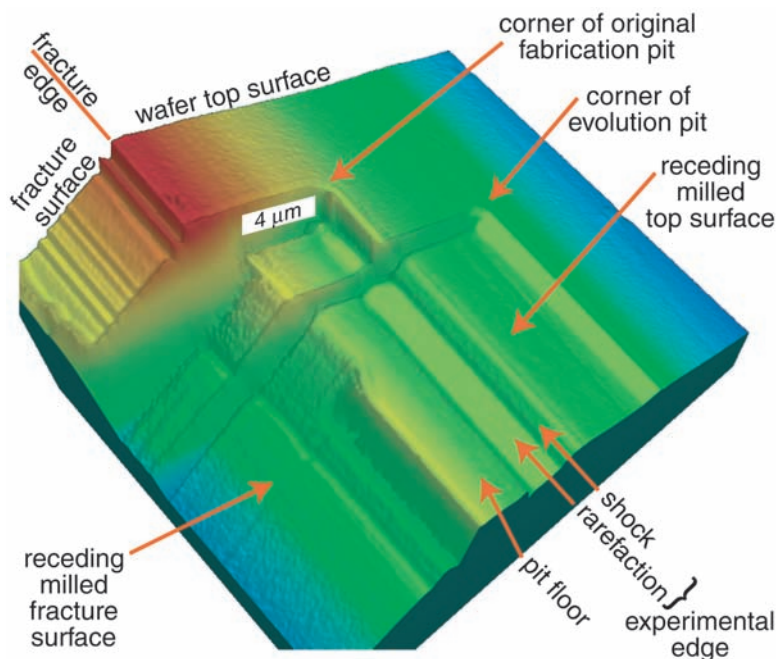


**Fig. 3.** Perspective view of pit milled by focused ion beam. The original fabrication pit had vertical side walls and straddles the fracture edge. Subsequently, the evolution pit was centered on the “experimental edge” of the original fabrication pit, causing edge morphology evolution. The original edge can be seen near corner of the original fabrication pit. As the evolution pit was milled, the original edge broke up into a steep side wall (“shock”) and shallower snail’s foot (“rarefaction”), as predicted. Note also the formation of another steep shock on the upper edge of the milled fracture surface, adjacent to the pit floor.

this case meant a 30-nm center-to-center spacing. The current profile within the beam is believed to be roughly Gaussian. We rastered various samples for varying durations.

The morphology evolution of the experimental edge was characterized using a Nanoscope OP 200M confocal optical profilometer (Hyphenated Systems, LLC, Burlingame, California). Relevant cross sections of the 3D images obtained are seen in the foreground of Fig. 4. These images provide compelling qualitative confirmation of the theory. In Fig. 4, the features of the profile of the experimental edge are, from right to left, the horizontal upper surface of the wafer that was milled vertically by rastering; a series of undulations that grew as the experimental edge was approached; a very steep edge corresponding to the undercompressive shock; a lower-slope rarefaction wave connecting the steep wall with the pit floor; a trough and ridge where the rarefaction wave intersects the pit floor; and a horizontal pit floor. As predicted (Fig. 2, A and B), with increasing fluence the height of the shock front gradually decreased, the size of the rarefaction wave gradually increased, and the steep slope did not dissipate. The undulations ahead of the shock front are related to surface diffusion and can be used to evaluate the diffusion parameter  $B$ . The valley and ridge at the intersection of the rarefaction wave and the pit floor are not predicted by the Sigmund mechanism; we expect that secondary collisions between scattered ions or recoiled atoms and

the surface are important here. Note, however, the shock that developed accidentally on the fracture surface, adjacent to the pit floor in Fig. 3. Whereas the shock on the “experimental edge” developed from a more steeply sloped feature, the shock on the fracture surface developed from a less steeply sloped feature, thereby confirming another prediction of the theory of a regime of feature “antidissipation”.

The ability to propagate sharp features without dissipation leads to the intriguing possibility of pre patterning a surface (by lithography or some other means) and then uniformly irradiating it to develop predetermined structures on an even smaller length scale (28). Directing two fronts toward each other might be exploited as a method of sublithographic patterning and may lead to new phenomena as well [e.g., (29)].

#### References and Notes

- M. J. Vasile, Z. Niu, R. Nassar, W. Zhang, S. Liu, *J. Vac. Sci. Technol. B* **15**, 2350 (1997).
- D. Adams, M. Vasile, T. Mayer, V. Hodges, *J. Vac. Sci. Technol. B* **21**, 2334 (2003).
- S. Facsko *et al.*, *Science* **285**, 1551 (1999).
- F. Frost, A. Schindler, F. Bigl, *Phys. Rev. Lett.* **85**, 4116 (2000).
- A. Cuenat, H. B. George, K. C. Chang, J. Blakeley, M. J. Aziz, *Adv. Mater.*, in press.
- J. Li *et al.*, *Nature* **412**, 166 (2001).
- D. Stein, J. Li, J. A. Golovchenko, *Phys. Rev. Lett.* **89**, 2761606 (2002).
- P. Sigmund, *Phys. Rev.* **184**, 383 (1969).
- P. Sigmund, *J. Mater. Sci.* **8**, 1545 (1973).
- R. M. Bradley, J. M. E. Harper, *J. Vac. Sci. Technol. A* **6**, 2390 (1988).
- R. Cuerno, A. L. Barabasi, *Phys. Rev. Lett.* **74**, 4746 (1995).
- G. Carter, V. Vishnyakov, *Phys. Rev. B* **54**, 17647 (1996).
- S. Park, B. Kahng, H. Jeong, A. L. Barabasi, *Phys. Rev. Lett.* **83**, 3486 (1999).
- J. Erlebacher, M. Aziz, E. Chason, M. Sinclair, J. Floro, *Phys. Rev. Lett.* **82**, 2330 (1999).
- J. Erlebacher, M. J. Aziz, E. Chason, M. B. Sinclair, J. A. Floro, *J. Vac. Sci. Technol. A* **18**, 115 (2000).
- S. Habenicht, *Phys. Rev. B* **63**, 125419 (2001).
- C. C. Umbach, R. L. Headrick, K. C. Chang, *Phys. Rev. Lett.* **87**, 246104 (2001).
- U. Valbusa, C. Boragno, F. B. de Mongeot, *J. Phys. Condens. Matter* **14**, 8153 (2002).

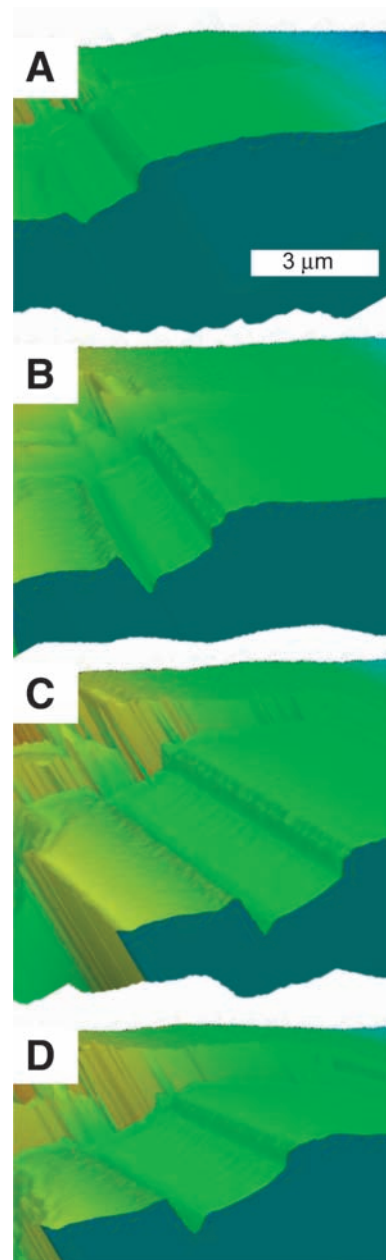


**Fig. 4.** Advancing pit as seen in experiment after (A) 128, (B) 256, (C) 384, and (D) 512 s, corresponding to fluences of  $0.6 \times 10^{18}$ ,  $1.2 \times 10^{18}$ ,  $1.8 \times 10^{18}$ , and  $2.4 \times 10^{18}$   $\text{Ga}^+$  ions/cm<sup>2</sup>. For ease of imaging, each sample was tilted arbitrarily before imaging; for comparison, the resulting images were rotated, so the sputtered top surface appears horizontal.

19. M. A. Makeev, R. Cuerno, A. L. Barabasi, *Nucl. Instrum. Methods Phys. Res. B* **197**, 185 (2002).
20. A. L. Bertozzi, A. Munch, X. Fanton, A. M. Cazabat, *Phys. Rev. Lett.* **81**, 5169 (1998).
21. J. Sur, A. L. Bertozzi, R. Behringer, *Phys. Rev. Lett.* **90**, 126105 (2003).
22. W. W. Mullins, *J. Appl. Phys.* **28**, 333 (1957).
23. J. F. Ziegler, J. P. Biersack, U. Littmark, *The Stopping and Range of Ions in Solids* (Pergamon, New York, 1985).
24. Details of the analysis are available as supporting material on Science Online.
25. G. B. Whitham, *Linear and Nonlinear Waves* (Wiley, New York, 1974).
26. A. L. Bertozzi, A. Munch, M. Shearer, *Physica D* **134**, 431 (1999).
27. A. L. Bertozzi, M. Shearer, *SIAM J. Math. Anal.* **32**, 194 (2000).
28. For a given lateral propagation distance, one would need to pattern features of a predictable minimum height.
29. M. Castro, R. Cuerno, L. Vazquez, R. Gago, *Phys. Rev. Lett.* **94**, 016102 (2005).
30. We are grateful to H. Bola George and W. MoberlyChan for technical assistance. This research was supported by Harvard Materials Research Science and Engineering Centers (MRSEC) grant NSF-DMR-0213805, U.S. Department of Energy grant DE-FG02-01ER45947 (O.A.U.), and NSF grants NSF-DMR-0306997 (M.J.A.)

and NSF-DMS-0296056 (M.P.B.). S.I. was partially supported by the Harvard College Research Fund. L.H.R. and S.I. were supported by the Research Experience for Undergraduates program (DMR-0353937) of the Harvard MRSEC.

**Supporting Online Material**  
[www.sciencemag.org/cgi/content/full/310/5746/294/DC1](http://www.sciencemag.org/cgi/content/full/310/5746/294/DC1)  
 SOM Text  
 Figs. S1 and S2  
 References

11 July 2005; accepted 29 August 2005  
 10.1126/science.1117219

# Structure and Freezing of MgSiO<sub>3</sub> Liquid in Earth's Lower Mantle

Lars Stixrude<sup>1\*</sup>† and Bijaya Karki<sup>2</sup>

First-principles molecular-dynamics simulations show that over the pressure regime of Earth's mantle the mean silicon-oxygen coordination number of magnesium metasilicate liquid changes nearly linearly from 4 to 6. The density contrast between liquid and crystal decreases by a factor of nearly 5 over the mantle pressure regime and is 4% at the core-mantle boundary. The ab initio melting curve, obtained by integration of the Clausius-Clapeyron equation, yields a melting temperature at the core-mantle boundary of 5400 ± 600 kelvins.

The structure of silicate liquids over most of the mantle pressure regime is unknown. There is experimental evidence that silicate liquid structure changes substantially on compression and that these changes include an increase in Si-O coordination number from 4 toward 6 (1), although there are no experimental observations within the liquid stability field at lower mantle pressure.

Most simulations of silicate liquids have been based on atomistic models, which permit much faster computation but have the disadvantage of being based on empirical force fields, the forms of which are uncertain (2, 3). First-principles molecular-dynamics (FPMD) simulations are considerably more costly because the electronic structure must be computed at each time step, but they are also more robust because they make no assumptions about the type of bonding or the shape of the charge density.

Here, we present FPMD simulations of MgSiO<sub>3</sub> liquid over the pressure-temperature range of Earth's mantle, based on density functional theory in the local density approximation and the plane-wave pseudopotential method (4). The simulations are performed in the canonical ensemble with periodic boundary conditions and a Nosé thermostat (5). The primary cell is cubic, with 80 atoms (16 formula

units). The initial condition is a pyroxene structure homogeneously strained to a cubic cell shape and the desired volume. The simulated strained crystal is melted at 6000 K and then cooled isochorically to 4000 K and 3000 K. Melting was confirmed by inspection of the radial distribution function and the mean square displacement. Total run durations are 3 ps, with the last 2.4 ps used for computing equilibrium averages. To ensure that the results are not sensitive to initial conditions, we performed simulations with twice the number of atoms (160 atoms initiated with a cubic majorite structure), twice the duration (6 ps), and different initial configurations (80-atom perovskite supercell homogeneously strained to a cubic cell shape) and found that the computed properties of the liquid were unchanged within statistical uncertainties. We explore a range of volumes  $V = V_x$  to  $V = V_x/2$ , where  $V_x = 38.9 \text{ cm}^3 \text{ mol}^{-1}$  is the experimental value for the liquid at the ambient-pressure melting point (1830 K) (6).

To explore freezing, we also performed simulations of orthorhombic MgSiO<sub>3</sub> perovskite, following the same procedures as the liquid simulations except that at each volume the shape of the unit cell was taken to be that found by structural relaxation at static conditions. We found that the unstrained perovskite structure persisted (meta) stably at all volumes  $V < 0.7V_x$ . We are thus able to compare directly the simulated properties of liquid and perovskite over the entire lower mantle pressure-temperature regime.

Inspection of the equilibrated liquid structure shows that compression has a large influence on the atomic arrangement (Fig. 1). At the exper-

imental zero-pressure volume, the liquid shows four-fold Si-O coordination, as does the stable crystalline phase at this volume, but without the elements of longer ranged order exhibited by the crystal, such as the infinitely long linear chains of tetrahedra that characterize pyroxenes. The liquid also shows a few non-four-fold-coordinated silicon atoms. At high pressure, the liquid structure is much more densely packed.

In the simulations, the average Si-O coordination number increased smoothly and nearly linearly with compression, with no discernible influence of temperature, reaching a value of 6 at a pressure corresponding to the base of Earth's mantle (Fig. 1). The coordination change does not take place over a narrow pressure interval, as has been suggested (7). Such a rapid structural change would be expected to cause changes in the compressibility of the liquid (7) and in the slope of the melting curve (8) over a correspondingly narrow pressure interval, anomalies for which we find no evidence in our simulations.

The liquid equation of state can be accurately described by the Mie-Grüneisen form

$$P(V, T) = P_c(V, T_0) + \frac{\gamma}{V} C_V (T - T_0) \quad (1)$$

where  $P_c$  is the reference isotherm, taken to be at  $T_0 = 3000 \text{ K}$ ,  $\gamma$  is the Grüneisen parameter, and  $C_V$  is the isochoric heat capacity. The latter quantities are computed from the simulations by noting that the internal energy  $E$  and pressure  $P$  vary linearly with temperature along isochores to within our uncertainty. The value of  $\gamma$  is then calculated at each volume from

$$\gamma = \frac{V}{C_V} \left( \frac{\partial P}{\partial T} \right)_V \quad (2)$$

and  $C_V = (\partial E / \partial T)_V$ . We find that  $C_V$  decreases by about 10% from  $4.12 \pm 0.11 \text{ Nk}$  at  $V = V_x$  [the experimental value is  $4.17 \pm 0.18 \text{ Nk}$  (9)] to  $3.54 \pm 0.11 \text{ Nk}$  at  $V = V_x/2$ , where  $N$  is the number of atoms and  $k$  is the Boltzmann constant.  $\gamma$  increases by a factor of three over the same range of volume, reflecting the increase in thermal pressure. All known mantle crystalline phases show the opposite behavior:  $\gamma$  decreases on compression (10).

The unusual behavior of  $\gamma$  in the liquid can be understood on the basis of the pressure-

<sup>1</sup>Department of Earth and Planetary Science, University of California, Berkeley, CA 94720, USA.

<sup>2</sup>Department of Computer Science, Louisiana State University, Baton Rouge, LA 70803, USA.

\*On leave from Department of Geological Sciences, University of Michigan, Ann Arbor, MI 48109, USA.

†To whom correspondence should be addressed. E-mail: stixrude@umich.edu

# 1 Supplementary Information

## 1.1 Yield correction

For a flat surface with constant but arbitrarily large slope

$$h(x) = bx + h_0,$$

the integral in the first equation of the main text with

$$E(x, x') = \frac{1}{(a\pi)^{3/2}\sigma\mu^2} \exp\left[-\frac{(x' - x)^2}{2\mu^2} - \frac{(h(x') - a - h(x))^2}{2\sigma^2}\right]. \quad (1)$$

can be exactly evaluated to be

$$\frac{\sqrt{2\pi}}{\sqrt{1 + b^2\frac{\mu^2}{\sigma^2}}} \exp\left[-\frac{a^2/\sigma^2}{2(1 + b^2\frac{\mu^2}{\sigma^2})}\right] \equiv I(b). \quad (2)$$

This expression has a simple interpretation. In the exponent, the slope  $b$  effectively reduces the penetration depth, because for off-normal incidence, the ion deposits its energy *closer* to the surface. Similarly, the  $b$  dependence in the prefactor is a correction to the ion flux due to the surface inclination.

The sputter yield is defined to be the number of atoms sputtered per incident ion. Because the ion flux is along the vertical direction, the sputter yield is proportional to the *vertical* rate of surface erosion,  $\dot{h}$ ; hence we multiply Eq. 2 by  $\sqrt{1 + b^2}$ , the denominator of the left hand side of equation (1) of the main text, and arrive at the sputter yield

$$\frac{Y(\theta)}{Y(0)} = \frac{\sqrt{1 + b^2}}{\sqrt{1 + b^2\frac{\mu^2}{\sigma^2}}} \exp\left[-\frac{a^2/\sigma^2}{2(1 + b^2\frac{\mu^2}{\sigma^2})} + \frac{a^2/\sigma^2}{2}\right], \quad (3)$$

where  $\theta$  is the angle between the ion trajectory and the surface normal, and  $b = \tan \theta$ . We have normalized this expression by the yield at normal incidence.

The dashed curve in Figure 1 shows the typical slope dependence of the sputtering yield from this model. For not too oblique incidence angles, this is consistent with experiments (1, 2), although for large slopes the yield diminishes, so that there is a peak at a high angle. Several authors (1, 3) have suggested the factor  $\exp(-\Sigma/\cos \theta) = \exp(-\Sigma\sqrt{1 + b^2})$  to correct for large incidence angles, where  $\Sigma$  can be interpreted as a fitting parameter. Then the normalized sputter yield becomes

$$\frac{Y(\theta)}{Y(0)} = \frac{\sqrt{1 + b^2}}{\sqrt{1 + b^2\frac{\mu^2}{\sigma^2}}} \exp\left[-\frac{a^2/\sigma^2}{2(1 + b^2\frac{\mu^2}{\sigma^2})} + \frac{a^2/\sigma^2}{2} - \Sigma(\sqrt{1 + b^2} - 1)\right]. \quad (4)$$

With three fitting parameters ( $a/\sigma$ ,  $\mu/\sigma$ ,  $\Sigma$ ), Eq. 4 is a reasonable analytic description of the experimental yield, as seen in Figure 1. We have found that the correction to the Sigmund

theory represented by  $\Sigma$  does not have any quantitative effect on the shocks described in this paper, and this correction does not appear in the main text discussion.

We note that there is a popular software package SRIM (Stopping and Range of Ions in Matter (4)), freely obtainable from <http://www.srim.org>, that estimates the parameters  $a, \mu, \sigma$  for various ions and targets. For the case of 30 keV gallium ions on silicon, SRIM gives a penetration depth of  $0.027\mu\text{m}$ . However, the values it gives for the energy distribution widths are inconsistent with our fitted ratios. The discrepancy is perhaps related to limitations in SRIM recently studied (5). We will use the fitted ratios and use  $a = 0.027\mu\text{m}$ , as a reference length when necessary.

The large angle correction should be taken as a phenomenological fitting function and not the unique expression from some underlying theory. For a crystalline target, it is expected that the crystallographic orientation with respect to the ion trajectory would affect the collision cascade, such as in surface channeling (6). But even for amorphous materials, the probability that an ion reflects off the surface rather than penetrates becomes significant at grazing angles. It has also been shown that under some conditions the radial distribution of deposited energy peaks at a finite distance from the ion trajectory, leading to a peak in the sputter yield at non-grazing angles (7). In any case, as we shall see, the results contained in subsequent sections follow from the fitted yield function itself and do not depend on these details.

Finally, it is also worth mentioning another type of correction to the yield that Sigmund's mechanism entirely neglects: the redeposition of sputtered atoms back onto the surface. Whether or not this is important depends on the detailed surface profile: if for example there is a wall facing a sputtered surface, it is clear that some of the sputtered atoms will be reflected back from the wall and affect the shape of the sputtered surface. We have taken great care to design our experiments to avoid this type of situation. In addition, the shape of the shock profile derived in this manuscript is essentially convex; in the absence of an opposing surface, the sputtered atoms will therefore not return to the surface.

## 1.2 Derivation of nonlinear PDE

In order to study the dynamics of surfaces, we need to describe surfaces that are not flat. Because we have seen that the Sigmund integral is Gaussian for a constant slope, we are led to consider a surface with slowly varying slope, in a sense to be made precise shortly. This will yield a local description of the Sigmund model as a partial differential equation (PDE). The novel feature of this PDE is that it describes surfaces of arbitrarily large slopes, as in the case of the pit edge.

Let's choose to calculate the surface velocity at  $x = 0$ , where the surface has the expansion

$$h(x) = h_0 + bx + \frac{\eta}{2}x^2 + \dots, \quad (5)$$

with slope  $b$  and second derivative  $\eta$  at the origin. We seek the correction to the flat surface evolution to leading order in  $\eta$ . Setting  $x = 0$  in the first equation in the main text and dropping

the prime in the dummy variable, the integral becomes

$$\int dx \exp \left[ -\frac{(bx - a + \eta x^2/2)^2}{2\sigma^2} - \frac{x^2}{2\mu^2} \right], \quad (6)$$

which to first order in  $\eta$  is

$$\int dx \exp \left[ -\frac{(bx - a)^2}{2\sigma^2} - \frac{x^2}{2\mu^2} \right] \left( 1 - \frac{\eta x^2}{2\sigma^2} (bx - a) \right). \quad (7)$$

This integral consists of a Gaussian multiplied by another function. If this function varies slowly over the width of the Gaussian, then our approximation is good, and we can neglect higher derivative terms in the Taylor expansion of  $h(x)$ . After completing the square in the exponent, the width  $\Delta$  of the Gaussian is found to be

$$\frac{1}{\Delta^2} = \frac{b^2}{2\sigma^2} + \frac{1}{2\mu^2}. \quad (8)$$

Note that this equation implies that  $\Delta < \sqrt{2}\mu$ , and thus as long as the radius of curvature of the surface is much longer than  $\mu$  the approximation is valid. The  $\eta$ -independent term is already shown in Eq. 2, while the order  $\eta$  integral evaluates to

$$\begin{aligned} & a\sqrt{\frac{\pi}{2}} \left( \frac{\mu^2}{\sigma^2} \right) \frac{-2b^4\mu^4/\sigma^4 + (a^2/\sigma^2 - 1)b^2\mu^2/\sigma^2 + 1}{(1 + b^2\mu^2/\sigma^2)^{7/2}} \exp \left[ -\frac{a^2/\sigma^2}{2(1 + b^2\mu^2/\sigma^2)} \right] \eta \\ & \equiv G(b) \eta. \end{aligned} \quad (9)$$

Using Eqs. 2 and 9, the surface evolution equation (second equation of the main text) becomes

$$\dot{h} = -Y(b) + D(b)h''(x), \quad (10)$$

where we have replaced  $\eta$  with  $h''(x)$  and restored the  $x$  dependence. The slope is now a local quantity:  $b(x) = h'(x)$ . We see that the surface evolution consists of a slope dependent erosion term and a curvature coefficient. The sputter yield

$$Y(b) \equiv \frac{pJ\epsilon}{2\pi\sigma} \sqrt{1 + b^2} e^{-\Sigma(\sqrt{1+b^2}-1)} I(b) \quad (11)$$

and the effective height ‘‘diffusivity’’

$$D(b) \equiv -\frac{pJ\epsilon}{\sigma} \frac{\sqrt{1 + b^2}}{2\pi} e^{-\Sigma(\sqrt{1+b^2}-1)} G(b). \quad (12)$$

Note that we have not made any restrictions on the magnitude of the slope, but have only required that  $\mu/R < 1$ , where  $R$  is the radius of curvature of the surface. Thus, as long as this criterion is satisfied, Eq. 10 is valid, even if the slope is *arbitrarily* high! Though we have chosen normal incidence, our formalism actually contains all incidence angles because any incidence angle can be brought to zero by suitably tilting the surface, that is, shifting the slope by a constant. Hence all of our results hold for any incidence angle through a rotation or projection. As described in the main text,  $D(b)$  is not always positive and is the origin of the Bradley-Harper instability (8).

### 1.3 Surface diffusion

The instability does not occur at arbitrarily small wavelengths. Surface diffusion dominates at sufficiently small distances, and together with the instability will select a finite wavelength. Surface diffusion is the result of random walks of mobile atoms, biased by changes in surface energy; in amorphous and other materials with thermodynamically rough surfaces, this is captured by the mean curvature.

According to the classic work of Herring and Mullins (9, 10), we can define a chemical potential on the surface

$$\mu = \kappa\gamma\Omega, \quad (13)$$

where  $\kappa$  is the mean curvature,  $\gamma$  is the surface-free energy per area, and  $\Omega$  is the molecular volume. By the Nernst-Einstein relation, a gradient of the chemical potential gives rise to a surface current of adatoms, given by

$$J = -\frac{D_s c}{kT} \nabla \mu = -\frac{D_s \gamma \Omega c}{kT} \nabla \kappa, \quad (14)$$

where  $D_s$  is the constant of surface diffusion,  $k$  is the Boltzmann constant,  $T$  is temperature, and  $c$  is the area density of mobile surface atoms. In almost all treatments,  $c$  is assumed to be a constant over the surface; that is, the mobile atoms that undergo diffusion comprise a uniform outer layer.

For pure surface diffusion, mass conservation requires that the normal velocity of a surface element,  $v_n$ , is equal to the divergence of  $-J$ , with an additional factor of the molecular volume. So the surface evolution is described by

$$v_n = \frac{D_s \gamma \Omega^2 c}{kT} \nabla^2 \kappa \equiv B \nabla^2 \kappa. \quad (15)$$

Note that in the context of surface transport the gradient operator  $\nabla$  is that associated with the surface. If our surface is described by a height function  $h(x)$ , then the surface gradient is

$$\nabla = \frac{1}{\sqrt{1+h_x^2}} \frac{\partial}{\partial x}. \quad (16)$$

Finally, the mean curvature is given by

$$\kappa = -\frac{h_{xx}}{(1+h_x^2)^{3/2}}. \quad (17)$$

Putting everything together, the evolution of the surface due to both sputtering (Eq. 10) and surface diffusion is given by

$$\frac{\partial h}{\partial t} = -Y(h_x) + D(h_x)h_{xx} - B \frac{\partial}{\partial x} \frac{1}{\sqrt{1+h_x^2}} \frac{\partial}{\partial x} \frac{h_{xx}}{(1+h_x^2)^{3/2}}. \quad (18)$$

The constant  $B$  is defined in Eq. 15.

## 1.4 Comparison to Sigmund model

We need to determine how effectively our nonlinear partial differential equation describes the full Sigmund theory (Eq. 1 in the main text) under typical conditions in the experiments.

We simulate the Sigmund dynamics by performing the integration using Simpson's rule and solving the fourth order surface diffusion semi-implicitly. A comparison between the full model and the reduced equation is shown in Figure 2. The agreement is excellent. The excellent agreement between the simulations is not affected if we simply neglect the  $D(b)$  term from Eq. 2; this is the reason for our assertion that the Bradley-Harper curvature coefficient is unimportant for the shocks described in this paper.

## 1.5 Derivation of Travelling Wave Solutions

Here we present a derivation of the travelling wave solutions. To study the propagating solutions of the third equation in the main text, we take  $b(x, t) = S(x - Ut)$ , where  $U$  is the propagation velocity. The numerical simulations indicate we should look for solutions that have zero slope on the right ( $b(x \rightarrow \infty) \rightarrow 0$ ) and fixed positive slope on the left ( $b(x \rightarrow -\infty) \rightarrow b_-$ ). Using this ansatz then gives

$$U = \frac{Y(b_-) - Y(0)}{b_-}, \quad (19)$$

as well as the equation for the shock profile

$$US - [Y(S) - Y(0)] = B \left( \frac{1}{\sqrt{1 + S^2}} \left( \frac{S'}{(1 + S^2)^{3/2}} \right)' \right)'. \quad (20)$$

In shock dynamics equation (19) is referred to as the Rankine-Hugoniot condition. For classical shocks, the shock velocity  $U$  satisfies the Lax condition  $C(b_-) > U > C(0) = 0$ . The advection velocity of the rear (front) of the shock is faster (slower) than the shock speed, and the profile is “compressed” from both sides, and the diffusive term prevents the profile from becoming multi-valued.

When the Lax condition does not hold, shocks can still exist. However such undercompressive shocks (11, 12) do not exist for arbitrary slopes  $b_-$ . To see this in the context of the present problem, we examine solutions to the ordinary differential equation for the shock profile  $S(x - Ut) = S(\eta)$ : We need to find solutions that obey  $S(\eta \rightarrow \infty) = 0$  and  $S(\eta \rightarrow -\infty) = b_-$ . If we examine small deviations from the zero slope asymptotes,  $S(\eta) = 0 + \epsilon e^{\alpha\eta}$ , we find that  $\alpha^3 \propto (U - C(0))/B$ ; since  $C(0) = 0$  this leads to two complex roots with negative real parts and one with positive real part. One condition must be imposed on the solution to eliminate the positive root. On the other hand, a similar argument for  $\eta \rightarrow -\infty$  implies that there  $\alpha^3 \propto (U - C(b_-))/B$ ; but since  $U - C(b_-) > 0$  we again have one root with positive real part and two with negative real part. To eliminate the modes which grow at negative infinity we need two additional conditions on the solution. So a total of three boundary conditions is needed to eliminate exponential growth in both directions. Eq. 20 is third order, so we have

just enough boundary conditions. However, the traveling solution  $S(\eta)$  is also translation invariant, and since we've exhausted the boundary conditions, this is not possible in general. The only way that a solution can exist is that there exist particular value(s) of  $U$  ( $b_-$ ) where there is a translationally invariant solution. This is the selection mechanism for the shock velocity as evidenced in the dynamical simulations. Note that the same argument applied to the Lax shock implies that we do not need to adjust  $U$  to have a solution. The undercompressive nature of the shock and the diffusion being fourth order constitute necessary conditions for the selection mechanism.

As mentioned in the main text, we have conducted a numerical search for the selected velocity of the undercompressive shock (using the BVP4c solver in MATLAB), and found that such a solution exists for  $b_- = 3.89(\theta = 76^\circ)$ .

Finally, it is worth making one additional remark about the existence of undercompressive shocks: the fourth order diffusion constant  $B$  is phenomenological, in that during ion beam sputtering we are not guaranteed that the Herring and Mullins formula (Eq. (18)) will hold. One could legitimately ask whether ion beam sputtering could lead to an effective second order diffusion on the surface. Alternatively, one can ask how second order diffusion affects the existence of undercompressive shocks. It turns out that a sufficiently large second order diffusivity destroys the existence of undercompressive shocks (12). In the present problem, the second order diffusivity  $D$  must be much less than of order  $U^{2/3}B^{1/3}$ . The fact that self-sharpening occurs experimentally demonstrates that the experimental  $D$  must obey this bound.

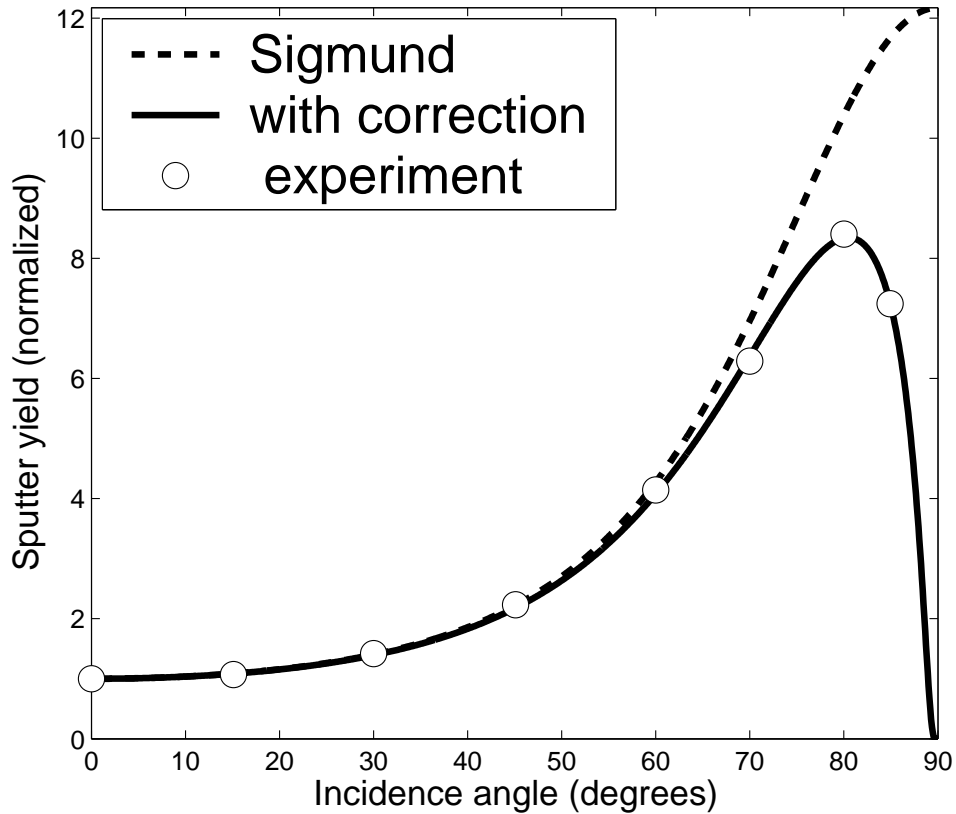


Figure 1: Angular dependence of sputtering yield. The yield is normalized by the normal incidence value. The parameters from fitting to the data are  $a/\sigma = 2.04$ ,  $\mu/\sigma = 0.658$ , and  $\Sigma = 0.0462$ . The data points are taken from Figure 2 in Vasile et al. (1), and fit to Eq. 4. The dashed curves is obtained by setting  $\Sigma = 0$ , leaving  $\mu/\sigma$  and  $a/\sigma$  unchanged.

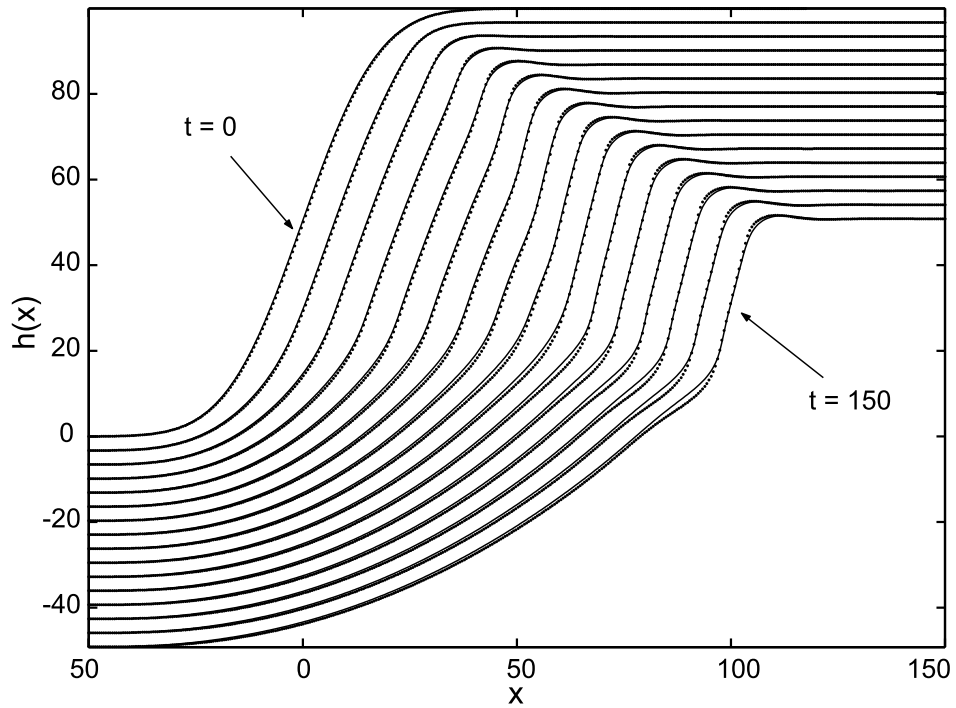


Figure 2: Surface evolution under the full Sigmund model (numerical solution of Eq. 1) (dotted) and the reduced PDE (Eq. 2) (solid). The agreement is excellent, and the discrepancy appears at later times in the high slope regions. The profiles are separated by time intervals of  $\Delta t = 10$ . The grid spacing is  $\Delta x = 0.5$  for both models. The initial profile is  $h = 50 \operatorname{erf}(x/20)$ .

## References

1. M. J. Vasile, J. Xie, and R. Nassar, *J. Vac. Sci. Technol. B* **17**, 3085 (1999).
2. G. A. Crow, Ph.D. thesis, Oregon Graduate Institute of Science and Technology (1990).
3. G. Falcone, *Phys. Rev. B* **33**, 5054 (1986).
4. J. F. Ziegler, J. P. Biersack, and U. Littmark, *The stopping and range of ions in solids* (Pergamon, 1985).
5. K. Wittmaack, *J. Appl. Phys.* **96**, 2632 (2004).
6. H. Winter, *Phys. Rep.* **367**, 387 (2002).
7. M. Feix, A. Hartmann, R. Kree, J. Munoz-Garcia, and R. Cuerno, *Phys. Rev. B* **71**, 125407 (2005).
8. R. M. Bradley and J. M. E. Harper, *J. Vac. Sci. Technol. A* **6**, 2390 (1988).
9. C. Herring, *J. Appl. Phys.* **21**, 301 (1950).
10. W. W. Mullins, *J. Appl. Phys* **28**, 333 (1957).
11. A. L. Bertozzi, A. Munch, and M. Shearer, *Physica D* **134**, 431 (1999).
12. A. L. Bertozzi and M. Shearer, *SIAM J. Math. Anal.* **32**, 194 (2000).